



# Photocatalytic H<sub>2</sub> production and CO<sub>2</sub> reduction on Cu, Ni-doped ZnO: effect of metal doping and oxygen vacancies

Ali M. Huerta-Flores<sup>1</sup> · E. Luévano-Hipólito<sup>2</sup> · Leticia M. Torres-Martínez<sup>1</sup> · A. Torres-Sánchez<sup>1</sup>

Received: 10 April 2019 / Accepted: 16 September 2019 / Published online: 20 September 2019  
© Springer Science+Business Media, LLC, part of Springer Nature 2019

## Abstract

Cu, Ni-doped ZnO materials were prepared through a fast and simple nitral-solution method. XRD and SEM studies confirmed the obtention of the hexagonal brucite structure of ZnO with hexagonal truncated-pyramid morphology. A slight decrease in the cell parameters of ZnO:Cu and ZnO:Ni was observed due to the incorporation in the crystal lattice of Cu<sup>2+</sup> and Ni<sup>2+</sup>. The absorption spectra of ZnO was red shifted in the doped samples. The formation of oxygen vacancies was confirmed through Raman and XPS spectroscopy, and it was found that the metal doping increased the oxygen vacancies in ZnO, being ZnO:Ni the sample that exhibited the higher density of oxygen vacancies. The photocatalytic activity of the samples was evaluated in the H<sub>2</sub> production and the reduction of CO<sub>2</sub> under UV light. ZnO:Cu and ZnO:Ni samples showed enhanced activity compared to pure ZnO in both photoreduction reactions. ZnO:Ni exhibited the highest photocatalytic activity (224 μmol g<sup>-1</sup> h<sup>-1</sup> H<sub>2</sub>, 29 μmol g<sup>-1</sup> h<sup>-1</sup> CH<sub>3</sub>OH), adjudicated to the major oxygen vacancies observed in this sample, which improved the charge separation and reduced the recombination of the photogenerated electron–hole pairs.

## 1 Introduction

The improvement and design of new technologies for the production of clean and renewable fuels and environmental protection is a central topic of research in these days [1]. Photocatalysis is a promising alternative with the capacity to solve environmental problems such as waste water [2], soil [3], air pollution [4], and to produce solar fuels including hydrogen and low carbon-based fuels, which can be

employed in fuel cells for the generation of electricity or to storage energy in the form of chemical bonds [5]. This easy and green technology offers multiple advantages, such as operating at room conditions and using abundant resources, including H<sub>2</sub>O, CO<sub>2</sub>, solar light and a photocatalyst without a negative impact in the environment. The photocatalyst can be reusable and has the capacity of: (i) promoting the elimination of dyes, antibiotics, pesticides, heavy metals, and other inorganic and organic hazardous compounds and (ii) convert the H<sub>2</sub>O and CO<sub>2</sub> molecules into solar-based fuels such as H<sub>2</sub>, CO, CH<sub>4</sub>, CH<sub>3</sub>OH, HCOOH, and HCHO [6].

Due to its outstanding and versatile optoelectronic properties, ZnO has been studied extensively in the literature [7]. ZnO shows a wide band gap (~3 eV) with direct transition [8], n-type conductivity [9], large exciton binding energy (60 meV) [10], strong oxidation ability [11], it is non-toxic, stable, abundant and can be easily prepared at low cost by a variety of methods, allowing a fine control of the microstructure, physicochemical and photocatalytic properties [12]. Also, the high surface reactivity of ZnO promotes the formation of defects originated from the oxygen non-stoichiometry [13]. The applications of ZnO include photocatalysis, photoelectrochemical cells, sensors, electrical devices, solar cells, diodes, supercapacitors, drug delivery, etc. [14].

On the other hand, an important disadvantage of ZnO involves a low quantum efficiency which originates a high

---

Ali M. Huerta-Flores and E. Luévano-Hipólito have contributed equally to this work.

---

**Electronic supplementary material** The online version of this article (<https://doi.org/10.1007/s10854-019-02204-0>) contains supplementary material, which is available to authorized users.

---

✉ Leticia M. Torres-Martínez  
leticia.torresgr@uanl.edu.mx; letorresg@yahoo.com

<sup>1</sup> Universidad Autónoma de Nuevo León, UANL, Departamento de Ecomateriales y Energía, Facultad de Ingeniería Civil, Av. Universidad S/N Ciudad Universitaria, C.P. 66455 San Nicolás de los Garza, Nuevo León, Mexico

<sup>2</sup> CONACYT - Universidad Autónoma de Nuevo León, UANL, Departamento de Ecomateriales y Energía, Facultad de Ingeniería Civil, Av. Universidad S/N Ciudad Universitaria, C.P. 66455 San Nicolás de los Garza, Nuevo León, Mexico

recombination rate, a short lifetime of the charge carriers, and low photon to electron conversion efficiency [15]. Multiple strategies have been employed to avoid this problem and to improve the electronic and optical properties of ZnO, in order to achieve an efficient separation and transport of the charge carriers. These strategies include the control of particle size [16], morphology [17], porosity [18], crystallinity [19], crystal facets [20], the formation of heterostructures [21], sensitizing with organic materials [22], doping with cations or anions [23], introducing intrinsic defects [24], among others. Doping is a strategy of particular importance due to it can improve the separation of the photogenerated charges, increase the surface area and conductivity, and reduce the band gap [24]. Doping with metal transition cations such as Fe, Cu, Ni, Co, and Mn induces the creation of energy levels in the electronic band structure that reduce the recombination of carriers and the band gap energy, causing a red shift in the absorption spectra [25]. The presence of defects on ZnO has been discussed in recent studies, due to they have a significant impact on the optical and electrical properties. Particularly, oxygen vacancies enhance the visible light absorption and reduce the recombination, acting as electron traps [26]. Inducing oxygen vacancies defects in the crystalline structure of ZnO through several methods of synthesis is a promising strategy to inhibit the charge recombination process, tune the electrical, optical and physicochemical properties of the material and improve the photocatalytic efficiency, though there are still many challenges on finding synthesis methods with the capacity to produce photocatalysts with appropriate properties at higher scale. Nital-solution is an innovative, simple, fast, and low-cost method that allows high yield and low temperature (180 °C) obtention of metal oxides with interesting physicochemical properties such as high crystallinity, controlled morphology and the formation of oxygen vacancies. This method involves several stages: (i) a condensation reaction of CH<sub>3</sub>OH and HNO<sub>3</sub> to form an ethyl nitrate, (ii) the addition of zinc acetate to the ethyl nitrate solution at 70 °C to generate a zinc intermediate, and (iii) the combustion reaction at 180 °C to produce ZnO [27]. So far, this synthesis method has not been employed for the preparation of ZnO doped with transition metals. In this work, it is proposed the synthesis of Cu, Ni-doped ZnO by the nital-solution method in order to promote oxygen vacancies formation. The photocatalytic activity of the materials was investigated in H<sub>2</sub>O and CO<sub>2</sub> reduction to produce H<sub>2</sub> and CH<sub>3</sub>OH, respectively. The influence of the dopant and oxygen vacancies on the physicochemical properties and the photocatalytic activity was also investigated. For the best of our knowledge, we report for the first time the use of nital-solution as a simple and low-temperature method, for the synthesis of Cu, Ni-doped ZnO exhibiting oxygen vacancies and enhanced photocatalytic activity for H<sub>2</sub> and CH<sub>3</sub>OH production compared to recent reports.

## 2 Experimental procedure

### 2.1 Synthesis of Cu,Ni-doped ZnO

The experimental procedure employed for the synthesis of ZnO by the nital-solution method was proposed in previous work [27]. The method involves the preparation of a solution of ethanol (96%) and HNO<sub>3</sub> in a 10:1 volume ratio in a round-bottom three necked flask, adapted with a conventional thermometer, a reflux system, and magnetic stirrer. The solution was heated at 70 °C, and the precursor of zinc (Zn(CH<sub>3</sub>COO)<sub>2</sub>·2H<sub>2</sub>O) was added. In the case of the doped materials, a 2% in weight of the doping cations was incorporated in the reaction media, using as precursors Cu(NO<sub>3</sub>)<sub>2</sub>·3H<sub>2</sub>O and Ni(NO<sub>3</sub>)<sub>2</sub>·6H<sub>2</sub>O, obtained from Sigma Aldrich with 99.99% of purity. The solution with the precursors was stirred and heated at 180 °C. At this temperature, the organic precursor overcomes the combustion reaction and form the pure ZnO and Cu,Ni-doped ZnO materials.

### 2.2 Characterization

The crystalline phases of all materials were characterized by X-ray diffraction (XRD) using a Bruker D8 Advance diffractometer with CuK $\alpha$  radiation ( $\lambda = 1.5406 \text{ \AA}$ ) operating at 40 kV and 40 mA, from 10° to 70° (2 $\theta$  angle) with a step of 0.01133° and a counting time of 0.3 s per step. Crystallite size was estimated from the XRD patterns using the Scherrer equation. Morphology and particle size were determined by Scanning Electron Microscopy (SEM) using a JEOL 6490 LV microscope coupled with Energy Dispersive X-ray Spectroscopy (EDS). A Thermo scientific XRD Raman microscope was employed to measure the Raman spectra of ZnO samples. All spectra were taken in the backscattering configuration at room temperature. XPS spectra were measured in an XPS-Auger Perkin Elmer PHY 560 spectrometer, with a monochromatic Al K $\alpha$  ( $h\nu = 1486.7 \text{ eV}$ ) X-ray source. Specific surface area ( $S_{\text{BET}}$ ) was obtained by N<sub>2</sub> physisorption at 77 K with a Belsorp II mini (Bel Japan), degassing the samples at 150 °C for 4 h before the analysis. Optical properties were analyzed from 200 to 800 nm using a UV-Vis NIR spectrophotometer (Cary 5000) coupled with an integration sphere for diffuse reflectance measurements. The band gap energy ( $E_{\text{g}}$ ) was calculated through the Kubelka–Munk function considering a direct transition for ZnO. Photoluminescence analysis was performed at room temperature in a fluorescence spectrophotometer (Cary Eclipse) integrated with a Xenon flash lamp. The samples were excited at 325 nm, using a scanning speed of 600 nm/min, and

an excitation width and emission slit of 5 nm. The FTIR spectra of the ZnO-based samples after the photocatalytic CO<sub>2</sub> reduction tests were measured in a range of 1800 to 800 cm<sup>-1</sup> on an FT-IR Nicolet iS50 equipment.

### 2.3 Photocatalytic activity

The photocatalytic experiments were performed separately in Batch Pyrex reactors at room temperature. For these experiments, 0.1 g of the material was suspended in 200 mL of deionized water. In the case of CO<sub>2</sub> photoreduction, CO<sub>2</sub> was injected in the reactor for 5 min, and the system was closed and pressurized at 2 psi and 20 °C. The reactors were irradiated with a UV lamp of 254 nm and 4400 μW/cm<sup>2</sup>. After 3 h of reaction, the gas and the liquid phase were analyzed by gas chromatography using a Trace Ultra Thermo Scientific equipment with a TCD and FID detector for H<sub>2</sub> and CH<sub>3</sub>OH quantification, respectively.

## 3 Results and discussion

### 3.1 X-ray diffraction

XRD patterns of the as-prepared materials are presented in Fig. 1. As can be observed in this figure, all the reflections correspond to the hexagonal brucite structure of ZnO, according to the JCPDS 36-1451 card. The samples exhibited well defined, sharp and intense reflections, due to their high crystallinity.

The crystallite size of the samples was calculated through the Scherrer equation; obtaining values in the range of 93 to 115 nm (Table 1). It was found that in the Cu and Ni-doped ZnO samples, the crystallite size tended to lower values, suggesting the incorporation of the cations in the brucite structure [28].

In ZnO:Cu sample, a peak of low intensity that could be associated to the presence of Cu<sub>2</sub>O (JCPDS card 05-0667) was observed, while in ZnO:Ni sample, no additional reflections were identified. This could be attributed, probably, to higher crystallinity of the CuO phase in comparison to NiO, which was not detected.

The cell parameters (*a*, *c*) of the samples were estimated from the XRD patterns, and they are presented in Table 1. According to the results, after the doping of ZnO with Ni and Cu the cell parameters exhibited a slight reduction, which can be associated with the introduction of the transition metal ions in the ZnO structure, due to the smaller ionic radii of Cu<sup>2+</sup> and Ni<sup>2+</sup> in comparison to Zn<sup>2+</sup>: Zn<sup>2+</sup> (74 pm) > Cu<sup>2+</sup> (71 pm) > Ni<sup>2+</sup> (69 pm) [29].

From these data, the *c/a* ratio in the hexagonal structure of ZnO was calculated, and the results are shown in Fig. 2. ZnO:Ni showed the lowest *c/a* ratio, which is related to a

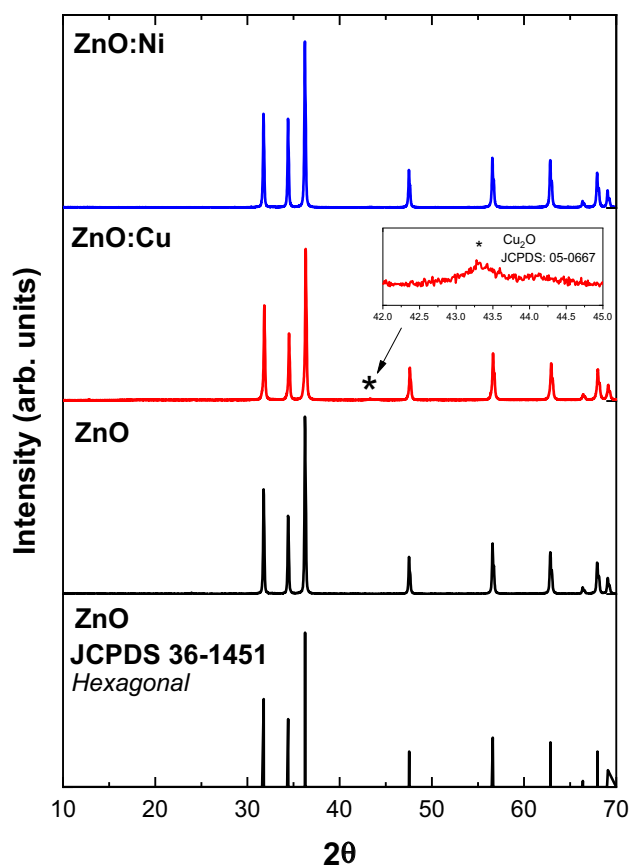


**Fig. 1** XRD patterns of ZnO-modified samples obtained by the nitral-solution method

**Table 1** Cell parameters from the ZnO-based materials prepared by the nitral-solution method

Sample	Crystallite size (nm)	<i>a</i> (Å)	<i>c</i> (Å)
ZnO	115	3.2532	5.2109
ZnO:Ni	93	3.2503	5.1992
ZnO:Cu	102	3.2532	5.2110

higher contribution of the (002) plane in the brucite structure. In the literature, a higher proportion of this plane in ZnO has been associated with an improvement in the electrical conductivity, optical properties, and the presence of oxygen vacancies [30].

### 3.2 Raman spectroscopy

Raman spectroscopy was used to study local structural changes in the brucite structure. These results are shown in Fig. 3a. In the Raman spectra, a typical ZnO spectrum was observed, composed mainly of four peaks [31]. The first peak (99 cm<sup>-1</sup>) (E<sub>2</sub> low) is dominated by vibrations of the

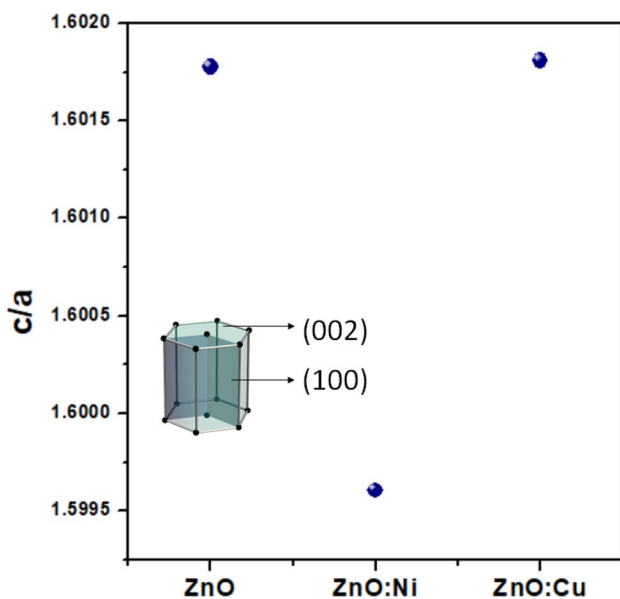


Fig. 2 Ratio  $c/a$  of pure ZnO and Cu, Ni-doped ZnO samples

Zn-sublattice, while the second peak ( $437\text{ cm}^{-1}$ ) ( $E_2$  high) corresponds to oxygen atoms. The peaks appearing around  $330$  and  $380\text{ cm}^{-1}$  are related to the second order and  $A_1$  (TO) mode in ZnO, respectively. In particular, the  $E_2$  high signal has been associated with oxygen vacancies [32, 33]. The area of each signal was modified after the incorporation of  $\text{Ni}^{2+}$  and  $\text{Cu}^{2+}$  to ZnO. The Raman shift of  $E_2$  low and high modes of each sample was analyzed to study the influence of the doping cations. As can be seen in Fig. 3b, the frequency of both  $E_2$  signals shifts to lower values after the incorporation of Cu and Ni and this effect is higher in the ZnO:Ni sample, suggesting a higher amount of oxygen vacancies in this sample.

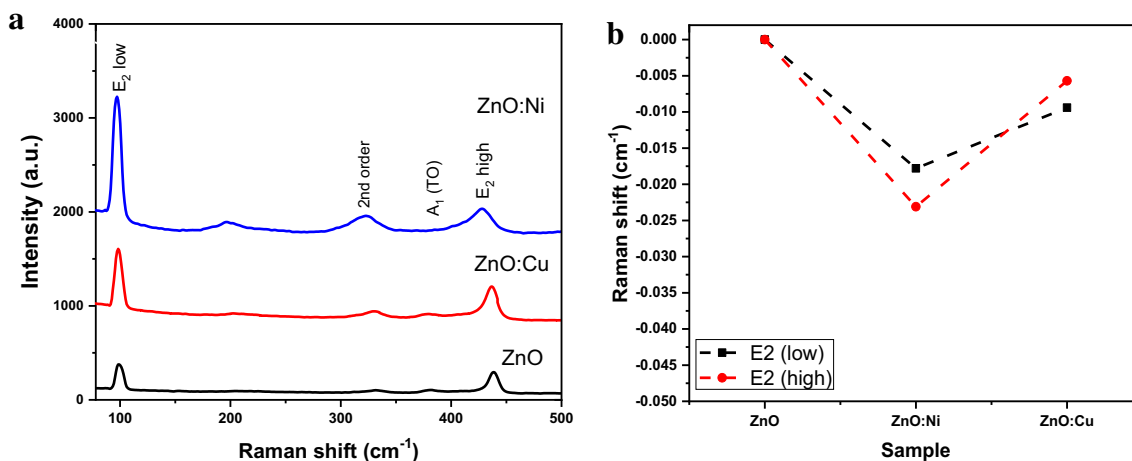


Fig. 3 **a** Raman spectra of ZnO-based samples and **b** Raman shift of the  $E_2$  (low) and (high) phonon modes

### 3.2.1 Mechanism of formation of oxygen vacancy formation in ZnO

The incorporation of  $\text{Cu}^{2+}$  and  $\text{Ni}^{2+}$  metal transition ions in ZnO crystal lattice promotes the formation of oxygen vacancies through the distortion of the crystalline structure originated by the difference in the ionic radius of  $\text{Zn}^{2+}$  in comparison to  $\text{Cu}^{2+}$  and  $\text{Ni}^{2+}$ . It is suggested that the introduction of metal transition ions reduce the formation energy of oxygen vacancies in ZnO. A mechanism of charge compensation is involved, where the holes formed by the metal doping are occupied by the electrons liberated by the oxygen vacancies for maintaining the charge neutrality. In addition, the generation of oxygen vacancies in the ZnO structure can be related to the highly exothermic nature of the synthesis employed. In this method, a high amount of gaseous by-products is liberated in an extremely short period of time, which could release the oxygen from the reaction media. These conditions also can promote the oxygen diffusion from the lattice, leaving oxygen vacant sites in the ZnO structure.

### 3.3 Scanning electron microscopy

Figure 4 shows the SEM micrographs of the ZnO samples. The morphology of pure ZnO resulted in hexagonal truncated-pyramids of size around  $5\text{ }\mu\text{m}$  (Fig. 4a). Cu, Ni-doped ZnO samples (Fig. 4d, g) showed no significant change in the morphology. It is worth mentioning that a slight decrease in the particle size was observed in the modified samples, probably, due to the incorporation of the transition metal ions. To corroborate the presence of Cu and Ni, elemental mappings and EDS analysis of the samples were performed, and they are shown in Fig. 4b–i. According to these results, Ni and Cu were identified in the doped samples, exhibiting a good dispersion and

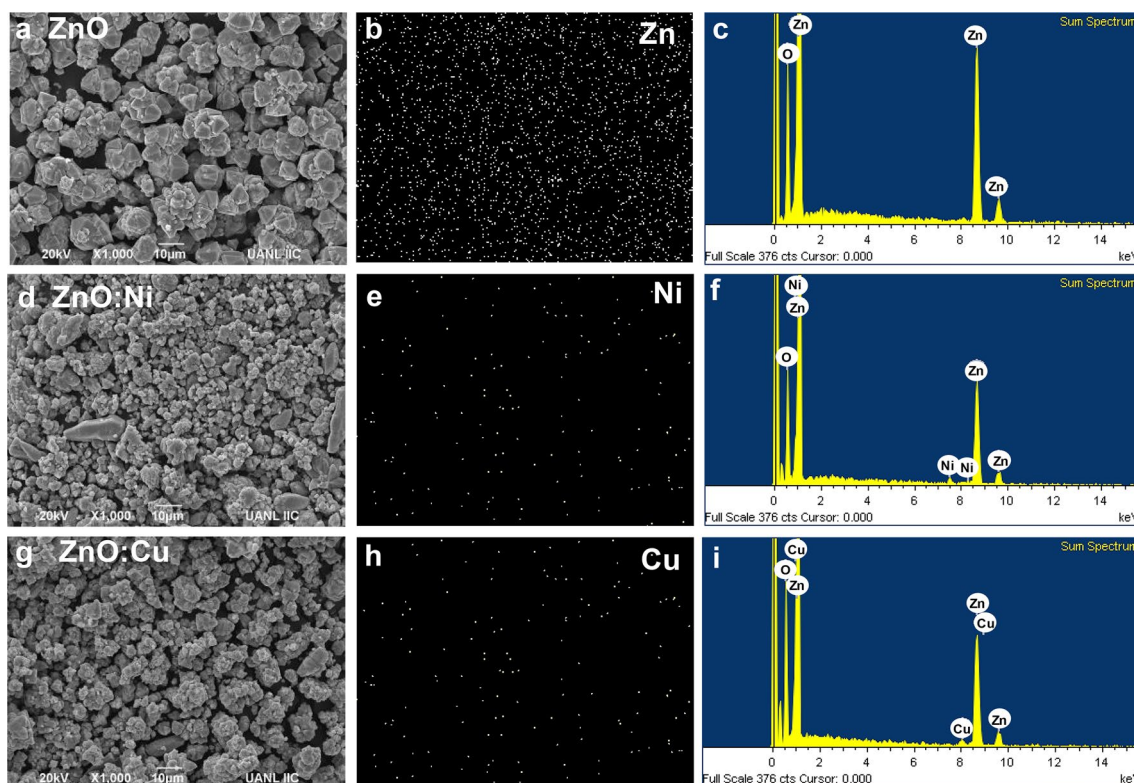


**Fig. 4** SEM images, elemental mapping and EDS analysis of (a–c) ZnO, (d–f) ZnO:Ni, and (g–i) ZnO:Cu samples

confirming the efficiency of the nitral-solution method for the modification of ZnO with transition metals. The results of the quantitative analysis by EDS of the samples are included in Tables S1, S2 and S3 in Supporting Information, showing an atomic content of Ni of 0.21% in the ZnO-Ni sample, while the sample ZnO-Cu sample exhibited a 0.38% atomic weight of Cu. Meanwhile, the Zn atomic content in the pure ZnO sample is higher (50.00%) in comparison to the ZnO-Ni sample (49.79%) and ZnO-Cu (49.62%).

### 3.4 N<sub>2</sub> physisorption

The profile of N<sub>2</sub> isotherms of all samples are shown in Fig. 5, and they correspond to type-III according to the IUPAC classification [34]. This type of profile corresponds with non-porous materials and denotes the low energy of adsorption. From these data, the BET surface areas of the samples were obtained, and they are shown in Table 2. In a general way, no significant changes in the surface area after the incorporation of the transition metal cations in ZnO were observed. The surface area of all the samples was lower than 8 m<sup>2</sup> g<sup>-1</sup>.

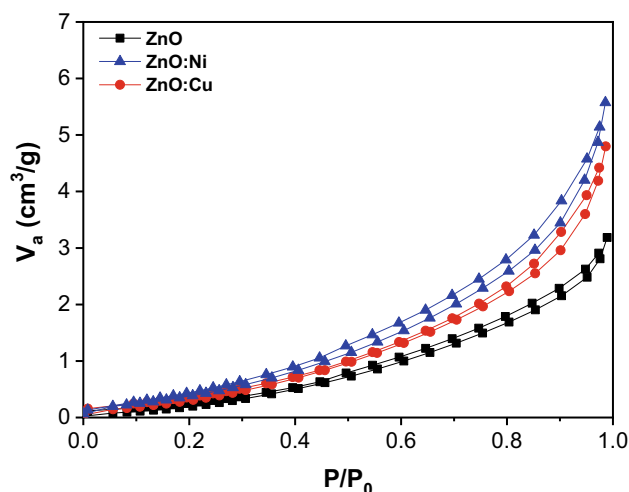


**Fig. 5** N<sub>2</sub> isotherms of ZnO, ZnO:Ni and ZnO:Cu samples obtained by the nitral-solution method

### 3.5 UV–Vis spectroscopy

The optical properties of the ZnO-based samples were studied by UV–Vis diffuse reflectance spectroscopy. The optical absorption, the Tauc plots and the band gap values of the samples calculated are shown in Fig. 6a–b and

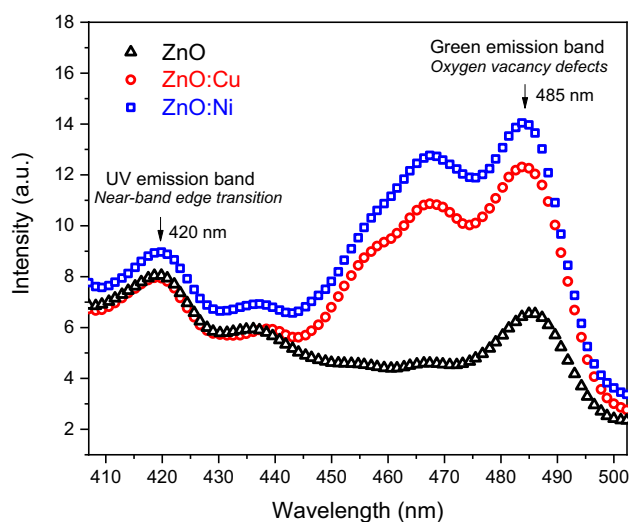
**Table 2** Optical and textural properties of the Cu,Ni-doped ZnO samples

Samples	$S_{BET}$ (m <sup>2</sup> g <sup>-1</sup> )	Band gap (eV)
ZnO	< 8	3.1
ZnO:Cu		2.8
ZnO:Ni		2.5

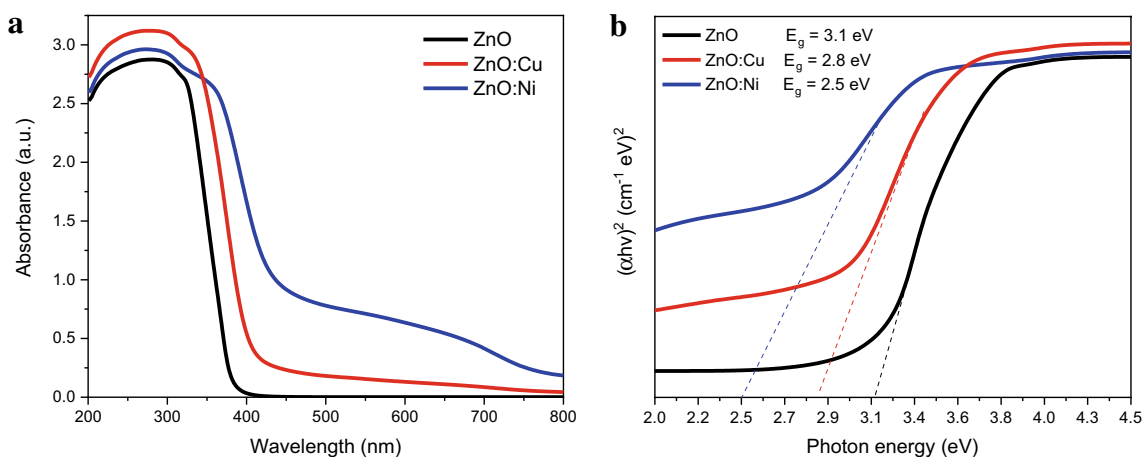
Table 2. The band gap energy ( $E_g$ ) was calculated from the Tauc plots, considering a direct transition for ZnO samples. The spectra of bare ZnO shows a characteristic absorption at around 400 nm. This absorption is assigned to the electron transition from the valence to the conduction band in ZnO ( $O_{2p} \rightarrow Zn_{3d}$ ) [35, 36]. The absorption onset of ZnO (400 nm) is shifted to longer wavelengths in the samples doped with Cu (443 nm) and Ni (496 nm), reducing the band gap from 3.1 eV in bare ZnO to 2.8 eV in ZnO:Cu and 2.5 eV in ZnO:Ni. The red shift in the absorption edge and the reduction in the band gap induces visible-light absorption in the doped samples, and it is originated from the incorporation of Ni and Cu in the ZnO lattice and the formation of band impurity levels [1, 37]. The optical spectra evidence the induced visible-light absorption in doped-ZnO samples, while bare ZnO only exhibits absorption in the UV range. This indicates a higher ability of doped-ZnO samples to harvest the solar spectrum and produce a higher number of photogenerated charges.

### 3.6 Photoluminescence spectroscopy

Room temperature photoluminescence spectra of ZnO pure and modified with Ni and Cu are showed in Fig. 7. The spectra of the samples exhibit a small peak centered at 420 nm. This UV emission is attributed to the near band-edge

**Fig. 7** Room temperature photoluminescence emission spectra of ZnO, ZnO:Cu and ZnO:Ni samples excited at 325 nm

transition from the conduction band to the valence band of ZnO and is related with the electron concentration [37, 38]. The UV-emission peak of the samples modified with Cu and Ni shows a slight redshift, associated to the  $sp-d$  interactions between the electrons in the band and the localized  $d$  electrons of Ni and Cu ions substituting Zn in the crystal lattice, originating a reduction of the band gap [39]. A green emission centered at 485 nm is adjudicated to the oxygen vacancies present in ZnO [40], and it is generated from the electron transference of Zn interstitial atoms to the neighbor oxygen vacancies [41]. An additional emission band around 467 nm is observed in Cu and Ni doped-ZnO samples, and this suggests the presence of other defect related states. As can be appreciated in Fig. 7, the green emission increases in doped-ZnO compared to bare ZnO, which could be related to

**Fig. 6** a UV-Vis diffuse reflectance spectroscopy analysis and b Tauc plot of the samples

an increase in the oxygen vacancies in the modified samples for the substitution of Zn by Cu and Ni ions. It is reported that the presence of oxygen vacancies improves the electron–hole separation and reduces the charge recombination by capturing the electrons, resulting in increased efficiency of the redox processes [42].

### 3.7 X-ray photoelectron spectroscopy

The chemical states of Cu and Ni present in ZnO samples are analyzed according to the results of XPS measurements. Figure 8 shows the survey spectrum of ZnO pure and modified with Cu and Ni, where it is possible to observe the Zn 2*p*, O 1*s*, C 1*s* and Zn Auger peaks in the three samples, while in the samples modified with Cu and Ni, small peaks corresponding to Cu 2*p* and Ni 2*p* are observed.

Figure 9a, b shows the Zn 2*p* and O 1*s* spectra of pure ZnO. The Zn 2*p* spectrum exhibits two peaks at 1021 eV and 1044 eV, attributed to Zn 2*p*<sub>3/2</sub> and Zn 2*p*<sub>1/2</sub>, corroborating the presence of Zn<sup>2+</sup> [43]. The O 1*s* spectrum was deconvoluted into two peaks at 530 eV (O<sub>I</sub>) and 531.5 eV (O<sub>II</sub>), assigned to the O in ZnO and O in defective ZnO<sub>x</sub> [44], evidencing the existence of oxygen vacancies in ZnO prepared by nitral solution method. The O 1*s* spectrum of the samples ZnO-Cu and ZnO-Ni are showed in Fig. 9d, f,

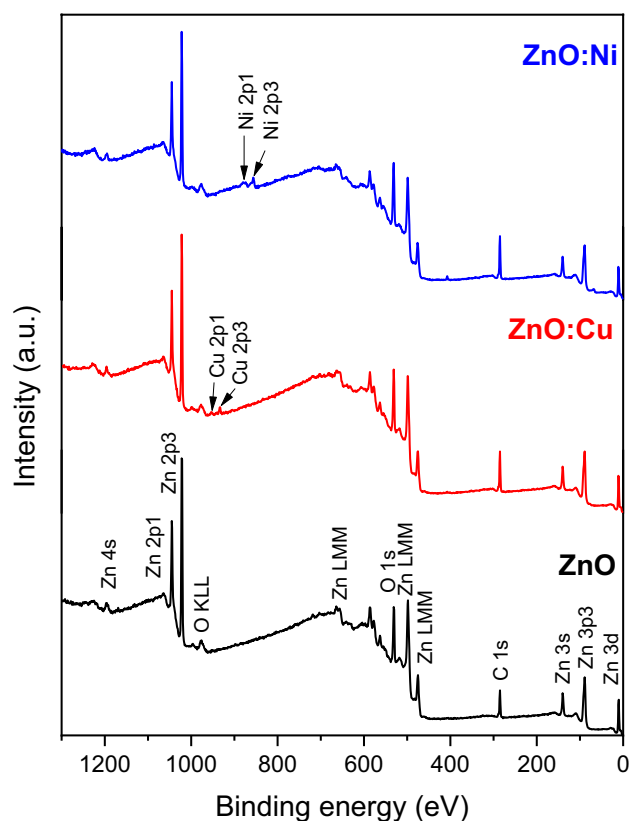


Fig. 8 Survey XPS spectra of the ZnO, ZnO-Cu and ZnO-Ni samples

respectively. The peak at around 530 eV (O<sub>I</sub>) is related to the O in ZnNiO and ZnCuO crystals, while the peak at 531.5 eV (O<sub>II</sub>) is associated with oxygen deficiencies in the samples. This component (O<sub>II</sub>) in ZnO-Ni sample increases in comparison with ZnO-Cu and ZnO, suggesting a higher amount of oxygen vacancies in ZnO-Ni sample.

Figure 9c, e shows the Cu 2*p* and Ni 2*p* spectra of the samples ZnO-Cu and ZnO-Ni. In the high-resolution Cu 2*p* spectra, shown in Fig. 9c, the peaks corresponding to the core levels of Cu 2*p*<sub>1/2</sub> and Cu 2*p*<sub>3/2</sub> are observed at 952.5 eV and 932.5 eV. Two satellite peaks at 943 eV and 960 eV indicate the presence of Cu<sup>2+</sup> in CuO [45]. The other two smaller peaks, observed at 932 eV and 951.5 eV reveal the presence of a small amount of Cu<sub>2</sub>O [46].

Figure 9e shows Ni 2*p* spectra. In this figure, we observe the Ni 2*p*<sub>3/2</sub> (855 eV) and Ni 2*p*<sub>1/2</sub> (872.5 eV) peaks and the satellite structures around 861 eV and 880 eV, respectively. These satellites are characteristic for nickel oxides and indicate that nickel exists in an oxygen environment in the sample [47]. The binding energy of Ni 2*p*<sub>3/2</sub> (855 eV) is similar to the reported for NiO [48]. No peaks corresponding to Ni<sup>0</sup> or Ni<sup>3+</sup> species were detected.

According to the results of the XPS analysis: (i) the ZnO samples prepared by nitral solution method exhibit oxygen vacancies, and the concentration is higher in ZnO-Ni sample, (ii) no Cu or Ni species in metallic form is observed in the samples, (iii) in the case of ZnO:Ni, only Ni<sup>2+</sup> is detected, while (iv) in the case of ZnO:Cu, Cu<sup>2+</sup> and Cu<sup>+</sup> (in a small proportion) are detected; this suggests the existence of Cu<sup>2+</sup>, Cu<sup>+</sup> and Ni<sup>2+</sup>.

The authors propose that the major difference in the ionic radii of Ni<sup>2+</sup> (69 pm) in comparison to Zn<sup>2+</sup> (74 pm) causes a higher lattice strain which induces the formation of a higher number of oxygen vacancies. The ionic radii difference between Cu<sup>2+</sup> (71 pm) and Zn<sup>2+</sup> (74 pm) is smaller, causing a lower amount of oxygen vacancies.

### 3.8 Photocatalytic activity

#### 3.8.1 H<sub>2</sub> production

The hydrogen evolution experiments were conducted for 3 h under UV light irradiation to evaluate the photocatalytic performance of the as-prepared samples. As it is displayed in Fig. 10, ZnO:Ni (224 μmol g<sup>-1</sup> h<sup>-1</sup>) and ZnO:Cu (206 μmol g<sup>-1</sup> h<sup>-1</sup>) showed more than 1.6 times H<sub>2</sub> production than pure ZnO (126 μmol g<sup>-1</sup> h<sup>-1</sup>) under the same experimental conditions. This reveals that the physical and chemical properties of the doped-samples promoted an increase in the activity by means of the oxygen vacancies and a longer lifetime of the charge carriers. ZnO:Ni sample exhibited the highest photocatalytic activity for hydrogen evolution, which was attributed to the higher amount of

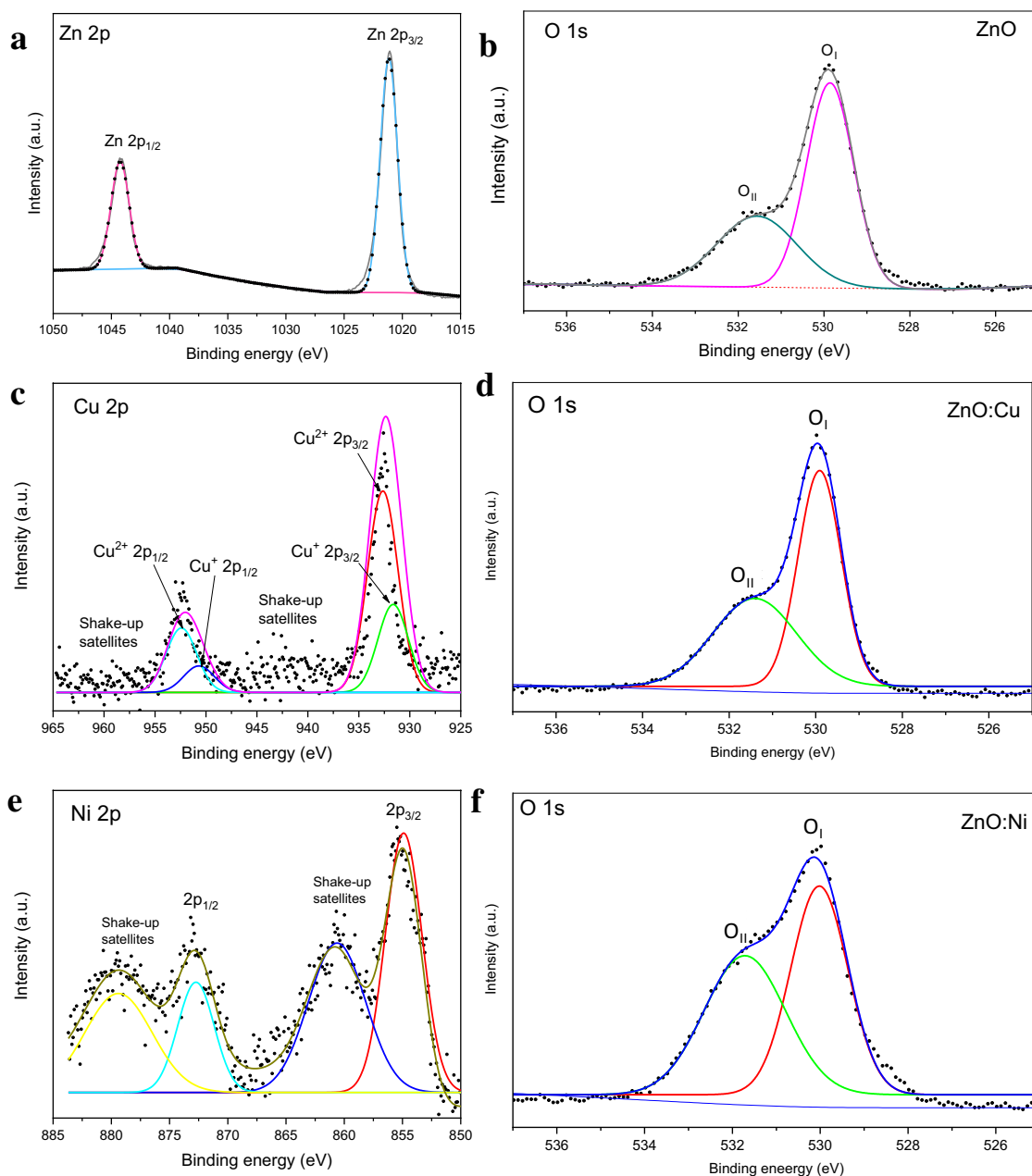


**Fig. 9** XPS spectra of the **a** Zn 2p and **b** O 1s in the ZnO sample; **c** Cu 2p and **d** O 1s in ZnO:Cu sample, and **e** Ni 2p and **f** O 1s in ZnO:Ni sample

oxygen vacancies in this sample, compared to ZnO:Cu and ZnO, as it was discussed in the Raman and XPS sections. This production is higher than previous reports of ZnO [49, 50], and it is a significant production in a system using pure water reaction media without the use of sacrificial agents.

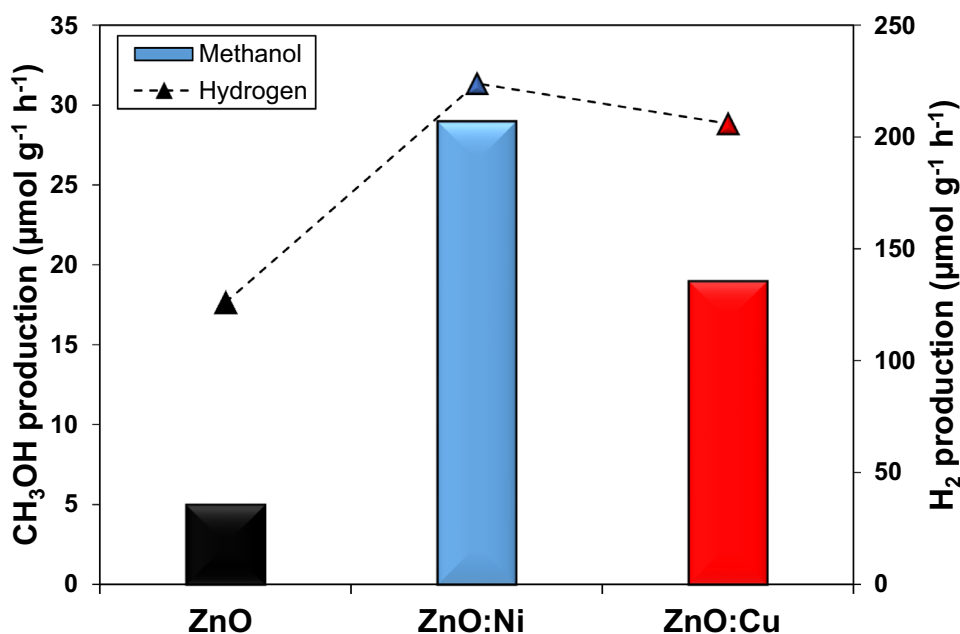
### 3.8.2 Methanol production

The results of the photocatalytic CO<sub>2</sub> reduction for methanol production are shown in Fig. 10. The

ZnO-based samples exhibited selectivity for CH<sub>3</sub>OH production, showing the following tendency: ZnO:Ni (29 μmol g<sup>-1</sup> h<sup>-1</sup>) > ZnO:Cu (19 μmol g<sup>-1</sup> h<sup>-1</sup>) > ZnO (5 μmol g<sup>-1</sup> h<sup>-1</sup>). An increase of 5.8 times the activity of pure ZnO was observed in the Ni-doped ZnO sample. The CH<sub>3</sub>OH generation exhibited the highest value using ZnO:Ni sample as the photocatalyst. This could be attributed to the highest CO<sub>2</sub> adsorption on the surface of ZnO:Ni. As it was discussed in the XPS section, the Cu,Ni-doped ZnO samples revealed the presence of



**Fig. 10** Methanol (*primary axis*) and hydrogen production (*secondary axis*) of the as-prepared samples after 3 h of irradiation



copper and nickel oxides on the surface of the material, which modifies the  $\text{CO}_2$  adsorption capacity of ZnO. It is reported that the surface modification with metal oxides is beneficial for  $\text{CO}_2$  adsorption, being this effect more favorable in surfaces modified with NiO in comparison to other oxides such as CuO,  $\text{Mn}_3\text{O}_4$ , and  $\text{CeO}_2$  [51].

The higher adsorption of  $\text{CO}_2$  in the ZnO:Ni was corroborated by FTIR analysis of the samples after the photocatalytic reaction (Supplementary Fig. S1). A characteristic band at  $1340 \text{ cm}^{-1}$  is attributed to the symmetric stretching of bent  $\text{CO}_2^-$  monodentate species [52]. The intensity of this band is higher in ZnO:Ni sample. Other bands at  $1410 \text{ cm}^{-1}$ , attributed to non-coordinated  $\text{CO}_3$  [53], and at  $950$  and  $875 \text{ cm}^{-1}$ , related to  $\text{O}=\text{C}=\text{O}$  bonds were also identified in the materials [54].

Another factor that can influence positively the  $\text{CO}_2$  adsorption in the samples is the presence of oxygen vacancies. These vacancies are related to a higher proportion of polar planes with high surface energy in the ZnO structure. The  $\text{CO}_2$  adsorption can be improved due to the stabilization of the surface energy on the polar faces of ZnO. This effect is accentuated in ZnO:Ni due to the highest amount of oxygen vacancies. According to previous reports, the adsorption of  $\text{CO}_2$  on ZnO faces with a high contribution of oxygen vacancies takes place by the interaction of  $p$  orbitals of  $\text{CO}_2$  with the ZnO valence band state [55]. Moreover, the highest reaction yield for methanol obtained herein is higher than the reported in previous works over ZnO pure and modified with other materials such as Cu,  $\text{Bi}_2\text{O}_3$ , and graphene [49, 56].

### 3.8.3 Photocatalytic mechanism

According to the characterization results, photocatalytic mechanisms are proposed for the processes of  $\text{CO}_2$  reduction (Fig. 11a) and  $\text{H}_2$  evolution (Fig. 11b). These mechanisms can be described in a general way as follows: first, the irradiation of the semiconductor with UV light conduces to the generation of electron and holes. The oxygen vacancies act as electron acceptors, and the intermediate energy levels introduced by the Cu and Ni doping enhance the separation of the charges and delay the recombination process [58]. Also, the oxygen vacancies improve the  $\text{H}_2\text{O}$  and  $\text{CO}_2$  adsorption in the photocatalysts, enhancing the interaction of electrons in the conduction band and holes in the valence band with the adsorbed molecules in the surface of the photocatalyst to perform the redox reactions, leading to the formation of  $\text{H}_2$  and  $\text{CH}_3\text{OH}$ .

More particularly, in pure ZnO, the oxygen vacancies ( $V_{\text{O}}$ ) are around  $0.9 \text{ eV}$  below the conduction band-edge, providing additional energy states that contribute to delay the recombination of electron and holes [49]. However, in the absence of a co-catalyst or a doping cation, the recombination occurs, decreasing the photocatalytic activity. In ZnO:Ni and ZnO:Cu samples, the metal doping induces a higher amount of oxygen vacancies, and the formation of metal oxides in the ZnO surface promotes a mechanism type-II for charge transfer between ZnO and the metal oxides, decreasing the recombination of the photogenerated charges effectively. Additionally, the  $\text{CO}_2$  adsorption is favored in the ZnO:Ni sample, enhancing the activation and

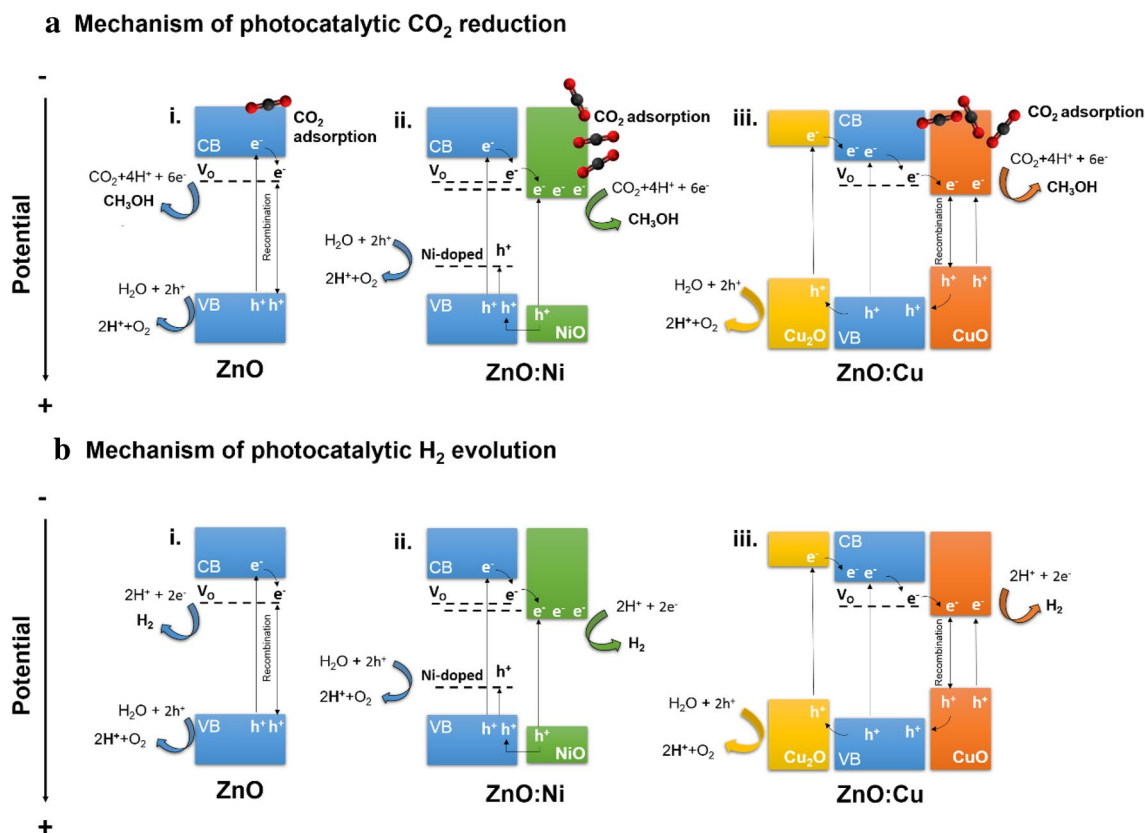


**Fig. 11** Photocatalytic mechanism of **a** CO<sub>2</sub> reduction and **b** H<sub>2</sub> evolution over (i) ZnO, (ii) ZnO:Ni, and (iii) ZnO:Cu samples.  $V_o$  denotes oxygen vacancies

conversion of CO<sub>2</sub> molecule to CH<sub>3</sub>OH. In ZnO:Cu sample, Cu<sub>2</sub>O and CuO are present on the surface of ZnO, favoring the electron migration from the conduction band of Cu<sub>2</sub>O to ZnO and CuO, while the holes are transported in the valence band in the opposite way.

In the photocatalytic H<sub>2</sub> production from pure water, the holes oxidize the H<sub>2</sub>O molecule to produce protons (H<sup>+</sup>), which react with the photogenerated electrons to form H<sub>2</sub>. In the case of the photocatalytic CO<sub>2</sub> reduction in H<sub>2</sub>O media, electrons are injected in CO<sub>2</sub> molecule to produce radicals that react with the H<sup>+</sup> from the oxidation of water to form CH<sub>3</sub>OH after a multielectron reduction process.

In summary, it was demonstrated that nital-solution method and metal doping promoted the formation of oxygen vacancies in ZnO crystal, acting as trap centers and inducing impurity levels in the electronic band structure, which reduced the recombination of electron and holes. A higher concentration of oxygen vacancies in ZnO:NiO, corroborated by Raman and XPS analysis, and the higher CO<sub>2</sub> adsorption in this sample, conducted to higher photocatalytic activity for solar fuels production.

A comparison of the efficiency exhibited by the materials developed in this work with related ZnO photocatalysts

reported in the literature is shown in Table 3. Though a direct comparison is difficult due to the use of different irradiation sources and reaction media, the activity of the ZnO-doped samples prepared herein by nital-solution method is high and competitive, considering that we employed a UV light source of low intensity (4400 μW) and no sacrificial agents or noble metal co-catalysts were incorporated.

As an advantage of this work, we use a simple and fast nital method for the preparation of the photocatalysts. This method uses a low-temperature of synthesis and allows adequate control of the metal doping. In the photocatalytic experiments, we don't use sacrificial agents, in comparison to other works. In this way, the cost of the process is reduced. Also, we use a lamp of lower intensity, which implies a lower consume of energy to perform the process. Moreover, the prepared materials showed a selective CO<sub>2</sub> reduction towards CH<sub>3</sub>OH production, which is an important feature for the development of green and alternative fuels.

**Table 3** Summary of the activities for H<sub>2</sub> and CH<sub>3</sub>OH production over ZnO-based photocatalysts reported in the literature compared to the materials developed in this work

Photocatalyst	Synthesis method	Product ( $\mu\text{mol g}^{-1} \text{h}^{-1}$ )	Reaction media	Irradiation source	Reference
ZnO	Solvothermal	503.88/CH <sub>3</sub> OH	Pure water, CO <sub>2</sub> , isopropanol	UV light 250 W	[51]
ZnSe		763.9/CH <sub>3</sub> OH			
ZnO-ZnSe		1581.82/CH <sub>3</sub> OH			
ZnO	Hydrothermal	0.09/ H <sub>2</sub> 0.03/ CH <sub>3</sub> OH	Pure water, CO <sub>2</sub>	UV light 8 W	[57]
ZnO-Cu		0.29/ H <sub>2</sub> 0.02/ CH <sub>3</sub> OH			
Bi <sub>2</sub> O <sub>3</sub> -Graphene-ZnO	Ultrasonication	5.531/ CH <sub>3</sub> OH 7.250/CH <sub>3</sub> OH	Pure water, CO <sub>2</sub> Pure water, CO <sub>2</sub> , Na <sub>2</sub> SO <sub>3</sub>	UV light 500 W	[59]
ZnO	Hydrothermal, impregnation	104/ H <sub>2</sub>	Pure water	UV light 4400 $\mu\text{W}$	[60]
ZnO-NiFe <sub>2</sub> O <sub>4</sub>		380/ H <sub>2</sub>			
ZnO-CuFe <sub>2</sub> O <sub>4</sub>		441/ H <sub>2</sub>			
ZnO	Hydrothermal	18.8/H <sub>2</sub> 60.2/CH <sub>3</sub> OH	Pure water, CO <sub>2</sub>	UV light 12 mW	[61]
ZnO-C		40.3/H <sub>2</sub> 430.2/CH <sub>3</sub> OH			
ZnO-Ag	Combustion	805/H <sub>2</sub>	Ethanol as sacrificial agent	UV, UV-Vis Hg-Xe lamp 300 W	[62]
ZnO-Cu	Thermal decomposition	1708.7/H <sub>2</sub>	KOH solution (0.5M) with H <sub>2</sub> S flow	UV, UV-Vis Xe lamp 450 W	[63]
ZnO-Ni	Auto-combustion	240/H <sub>2</sub>	Lactic acid as sacrificial agent	Xe lamp 300 W	[64]
ZnO	Nital-solution	126/H <sub>2</sub> 5/CH <sub>3</sub> OH	Pure water, CO <sub>2</sub> ,	UV light 4400 $\mu\text{W}$	This work
ZnO:Cu		206/H <sub>2</sub> 19/CH <sub>3</sub> OH			
ZnO:Ni		224/H <sub>2</sub> 29/CH <sub>3</sub> OH			

## 4 Conclusions

ZnO-based materials with oxygen vacancies were successfully synthesized by a simple and fast nital-solution method. The samples exhibited hexagonal brucite structure with crystallite sizes in the range of 93 to 115 nm. The incorporation of Cu and Ni ions in the ZnO lattice conducted to a reduction in the cell parameters and the band gap, an increase in the oxygen vacancies, a reduction of the recombination, and an improvement in the charge separation and the photocatalytic activity. The efficiency for H<sub>2</sub> and CH<sub>3</sub>OH production was influenced by the type of doping cation and oxygen vacancies. The highest H<sub>2</sub> and CH<sub>3</sub>OH production was obtained by ZnO:Ni (224  $\mu\text{mol g}^{-1} \text{h}^{-1}$  H<sub>2</sub>, 29  $\mu\text{mol g}^{-1} \text{h}^{-1}$  CH<sub>3</sub>OH), showing 5.8 and 1.6 times-fold higher performance, respectively, compared to bare ZnO. This enhancement could be attributed to the higher amount of oxygen vacancies in this sample and the intermediate energy levels by the metal doping that delay the recombination of the electron and hole pairs. Also, the thermodynamics of the adsorption-decomposition process over ZnO-Ni sample is more favorable, promoting a higher conversion efficiency. In summary,

these results highlight the potential application of the nital-solution method for the preparation of highly crystalline and efficient photocatalysts with tunable oxygen vacancies by metal doping for the production of solar fuels.

**Acknowledgements** The authors would like to thank CONACYT and UANL for the financial support for this research through the following projects: Cátedras CONACYT 1060, CONACYT-FC-1725, CONACYT-CB-2014-237049, CONACYT- CB-256795-2016, CONACYT- INFRA-2015-252753, CONACYT-PDCPN-2015-487, CONACYT-NRF-2016-278729SEP (PROFOCIE-2014-19-MSU0011T-1, PRODEP-103.5/15/14156), PAIFIC-UANL-2018-5, UANL PAICYT 2019 IT1021-19, UANL-CA-244 PROFIDES Desarrollo de materiales ambientales ID 63185, and FIC-UANL (PAIFIC/2018-5 and PAIFIC/2018-9). We are grateful to Dr. David Avellaneda Avellaneda for his help with XPS analysis.

## References

1. P.V. Radovanovic, D.R. Gamelin, High-temperature ferromagnetism in Ni<sup>2+</sup>-doped ZnO aggregates prepared from colloidal diluted magnetic semiconductor quantum dots. *Phys. Rev. Lett.* **91**(15), 157202 (2003)

2. H. Zangeneh et al., Photocatalytic oxidation of organic dyes and pollutants in wastewater using different modified titanium dioxides: a comparative review. *J. Ind. Eng. Chem.* **26**, 1–36 (2015)
3. A.N. Wang et al., Diphenylarsinic acid contaminated soil remediation by titanium dioxide (P25) photocatalysis: degradation pathway, optimization of operating parameters and effects of soil properties. *Sci. Total Environ.* **541**, 348–355 (2016)
4. V. Binas et al., Modified TiO<sub>2</sub> based photocatalysts for improved air and health quality. *J. Materiomics* **3**(1), 3–16 (2017)
5. Y.S. Chaudhary, *Solar Fuel Generation* (CRC Press, Boca Raton, 2017)
6. L. Wei et al., TiO<sub>2</sub>-based heterojunction photocatalysts for photocatalytic reduction of CO<sub>2</sub> into solar fuels. *J. Mater. Chem. A* **6**(45), 22411–22436 (2018)
7. J. Wang et al., Synthesis, properties and applications of ZnO nanomaterials with oxygen vacancies: a review. *Ceram. Int.* **44**(7), 7357–7377 (2018)
8. A.H. Ramelan et al., ZnO wide bandgap semiconductors preparation for optoelectronic devices. *IOP Conf. Ser.* **176**, 012008 (2017)
9. J. Kaupužs et al., Origin of n-type conductivity in ZnO crystal and formation of Zn and ZnO nanoparticles by laser radiation. *Opt. Laser Technol.* **111**, 121–128 (2019)
10. C. Klingshirn et al., Room-temperature stimulated emission of ZnO: alternatives to excitonic lasing. *Phys. Rev. B* **75**(11), 115203 (2007)
11. Z. Xin et al., Microwave-assisted hydrothermal synthesis of chrysanthemum-like Ag/ZnO prismatic nanorods and their photocatalytic properties with multiple modes for dye degradation and hydrogen production. *RSC Adv.* **8**(11), 6027–6038 (2018)
12. A. Naveed Ul Haq et al., Synthesis approaches of zinc oxide nanoparticles: the dilemma of ecotoxicity. *J. Nanomater.* (2017). <https://doi.org/10.1155/2017/8510342>
13. S. Repp, S. Weber, E. Erdem, Defect evolution of nonstoichiometric ZnO quantum dots. *J. Phys. Chem. C* **120**(43), 25124–25130 (2016)
14. U.M. Özgür, D. Hofstetter, H. Morkoç, ZnO devices and applications: a review of current status and future prospects. *Proc. IEEE* **98**, 1255–1268 (2010)
15. F.-R. Wang et al., Enhanced photoelectric properties by the coordinating role of doping and modification. *Phys. Chem. Chem. Phys.* **18**, 4850–4859 (2016)
16. A. Dodd et al., Effect of particle size on the photocatalytic activity of nanoparticulate zinc oxide. *J. Nanopart. Res.* **8**, 43–51 (2006)
17. C. Hu et al., Morphological controlled preparation and photocatalytic activity of zinc oxide. *Mater. Chem. Phys.* **217**, 182–191 (2018)
18. F. Xu et al., Hierarchically assembled porous ZnO nanoparticles: synthesis, surface energy, and photocatalytic activity. *Chem. Mater.* **19**(23), 5680–5686 (2007)
19. A.A.A. Ahmed et al., Improvement of the crystallinity and photocatalytic property of zinc oxide as calcination product of Zn–Al layered double hydroxide. *J. Alloy. Compd.* **539**, 154–160 (2012)
20. E. Debroye et al., Facet-dependent photoreduction on single ZnO crystals. *J. Phys. Chem. Lett.* **8**(2), 340–346 (2017)
21. E. Mendoza-Mendoza et al., One-step synthesis of ZnO and Ag/ZnO heterostructures and their photocatalytic activity. *Ceram. Int.* **44**(6), 6176–6180 (2018)
22. Z. Youssef et al., Dye-sensitized nanoparticles for heterogeneous photocatalysis: cases studies with TiO<sub>2</sub>, ZnO, fullerene and graphene for water purification. *Dyes Pigments* **159**, 49–71 (2018)
23. M.T. Taghizadeh et al., Ultrasonic-assisted synthesis of ZnO/NiO nanocomposites and kinetic study of their photocatalytic activity. *J. Mater. Sci.* **29**(2), 978–984 (2018)
24. M.K. Satheesan et al., Influence of defects on the photocatalytic activity of Niobium doped ZnO nanoparticles. *J. Mater. Sci.* **28**(6), 4719–4724 (2017)
25. M. Khairy, W. Zakaria, Effect of metal-doping of TiO<sub>2</sub> nanoparticles on their photocatalytic activities toward removal of organic dyes. *Egypt. J. Pet.* **23**(4), 419–426 (2014)
26. M. Shandrikov et al., Red shift of absorption spectra of metal-doped TiO<sub>2</sub> coatings. *J. Phys.* **1115**, 032055 (2018)
27. S. Kuriakose, B. Satpati, S. Mohapatra, Enhanced photocatalytic activity of Co doped ZnO nanodisks and nanorods prepared by a facile wet chemical method. *Phys. Chem. Chem. Phys.* **16**, 12741–12749 (2014)
28. C. Gomez-Solís et al., Rapid synthesis of ZnO nano-corncobs from Nital solution and its application in the photodegradation of methyl orange. *J. Photochem. Photobiol. A* **298**, 49–54 (2015)
29. R. Jeyachitra et al., Effect of Ni doping on structural, optical and photocatalytic properties of Zn 1-X Ni X O nanoparticles prepared by different pH conditions. *J. Adv. Chem.* **12**, 4097–4107 (2017)
30. M. Shamsipur et al., Ion imprinted polymeric nanoparticles for selective separation and sensitive determination of zinc ions in different matrices. *Spectrochim. Acta Part A* **117**, 24–33 (2014)
31. G.A. Velázquez-Nevárez et al., Optical and electrical properties of (002)-oriented ZnO films prepared on amorphous substrates by sol-gel spin-coating. *J. Mater. Res.* **19**, 113–117 (2016)
32. V. Russo et al., Multi-wavelength Raman scattering of nanostructured Al-doped zinc oxide. **115**(7), 073508 (2014)
33. H. Fukushima, et al. Evaluation of oxygen vacancy in ZnO using Raman spectroscopy. In 2015 Joint IEEE International Symposium on the Applications of Ferroelectric (ISAF), International Symposium on Integrated Functionalities (ISIF), and Piezoelectric Force Microscopy Workshop (PFM) (2015)
34. H. Fukushima et al., Evaluation of oxygen vacancies in ZnO single crystals and powders by micro-Raman spectroscopy. *J. Ceram. Soc. Jpn.* **125**, 445–448 (2017)
35. M. Thommes et al., Physisorption of gases, with special reference to the evaluation of surface area and pore size distribution (IUPAC Technical Report). *Pure Appl. Chem.* **87**, 1051–1069 (2015)
36. A.K. Zak et al., Effects of annealing temperature on some structural and optical properties of ZnO nanoparticles prepared by a modified sol-gel combustion method. *Ceram. Int.* **37**(1), 393–398 (2011)
37. C. Liu, T.R. Cundari, A.K. Wilson, CO<sub>2</sub> reduction on transition metal (Fe Co, Ni, and Cu) surfaces: in comparison with homogeneous catalysis. *J. Phys. Chem. C* **116**(9), 5681–5688 (2012)
38. D. Anbuselvan, S. Muthukumar, Defect related microstructure, optical and photoluminescence behaviour of Ni, Cu co-doped ZnO nanoparticles by co-precipitation method. *Opt. Mater.* **42**, 124–131 (2015)
39. T.M. Hammad et al., Optical and magnetic properties of Cu-doped ZnO nanoparticles. **24**(8), 2846–2852 (2013)
40. J.K. Salem, T.M. Hammad, R.R. Harrison, Synthesis, structural and optical properties of Ni-doped ZnO micro-spheres. *J. Mater. Sci.* **24**(5), 1670–1676 (2013)
41. A. Tarat et al., Microwave-assisted synthesis of layered basic zinc acetate nanosheets and their thermal decomposition into nanocrystalline ZnO. *Nanoscale Res. Lett.* **9**(1), 11 (2014)
42. R. Bhaskar et al., Mechanism of green luminescence in ZnO. *Indian J. Pure Appl. Phys.* **47**, 772–774 (2009)
43. Q. Zhang et al., Oxygen vacancy-mediated ZnO nanoparticle photocatalyst for degradation of methylene blue. *Appl. Sci.* **8**, 353 (2018)
44. A.A. Mosquera et al., Exciton and core-level electron confinement effects in transparent ZnO thin films. *Sci. Rep.* **3**, 1714 (2013)
45. I.G. Morozov et al., Structural, optical, XPS and magnetic properties of Zn particles capped by ZnO nanoparticles. *J. Alloys Compd.* **633**, 237–245 (2015)
46. L. Hu et al., Catalytic epoxidation of stilbene with FePt@Cu nanowires and molecular oxygen. *Chem. Commun.* **46**(45), 8591–8593 (2010)

47. X. Deng et al., Low-temperature solution synthesis of CuO/Cu<sub>2</sub>O nanostructures for enhanced photocatalytic activity with added H<sub>2</sub>O<sub>2</sub>: synergistic effect and mechanism insight. *RSC Advances* **7**(8), 4329–4338 (2017)
48. A.P. Grosvenor et al., New interpretations of XPS spectra of nickel metal and oxides. *Surf. Sci.* **600**(9), 1771–1779 (2006)
49. S. Uhlenbrock et al., The influence of defects on the Ni 2p and O 1s XPS of NiO. *J. Phys.* **4**(40), 7973–7978 (1992)
50. Y. Peng et al., Stable yellow ZnO mesocrystals with efficient visible-light photocatalytic activity. *CrystEngComm* **16**(34), 7906–7913 (2014)
51. S. Zhang, X. Yin, Y. Zheng, Enhanced photocatalytic reduction of CO<sub>2</sub> to methanol by ZnO nanoparticles deposited on ZnSe nanosheet. *Chem. Phys. Lett.* **693**, 170–175 (2018)
52. M. Li et al., Effect of metal oxides modification on CO<sub>2</sub> adsorption performance over mesoporous carbon. *Microporous Mesoporous Mater.* **249**, 34–41 (2017)
53. F. Solymosi, The bonding, structure and reactions of CO<sub>2</sub> adsorbed on clean and promoted metal surfaces. *J. Mol. Catal.* **65**(3), 337–358 (1991)
54. W.N.R.W. Isahak et al., Adsorption–desorption of CO<sub>2</sub> on different type of copper oxides surfaces: physical and chemical attractions studies. *J. CO<sub>2</sub> Util.* **2**, 8–15 (2013)
55. T. Parvin et al., Photocatalytic degradation of municipal wastewater and brilliant blue dye using hydrothermally synthesized surface-modified silver-doped ZnO designer particles. *Int. J. Photoenergy* **670610**, 1–8 (2012)
56. S. Farias et al., CO<sub>2</sub> adsorption on polar surfaces of ZnO. *J. Mol. Model.* **19**(5), 2069–2078 (2012)
57. J. Núñez et al., Effect of copper on the performance of ZnO and ZnO<sub>1-x</sub>N<sub>x</sub> oxides as CO<sub>2</sub> photoreduction catalysts. *Catal. Today* **209**, 21–27 (2013)
58. Q. Ma et al., Cu doped ZnO hierarchical nanostructures: morphological evolution and photocatalytic property. *J. Mater. Sci.* **30**(3), 2309–2315 (2019)
59. A. Ali, M.R. Biswas, W.C. Oh, Novel and simple process for the photocatalytic reduction of CO<sub>2</sub> with ternary Bi<sub>2</sub>O<sub>3</sub>–graphene–ZnO nanocomposite. *J. Mater. Sci.* **29**(12), 10222–10233 (2018)
60. A. Soto-Arreola et al., Improved photocatalytic activity for water splitting over MFe<sub>2</sub>O<sub>4</sub>–ZnO (M = Cu and Ni) type-II heterostructures. *J. Photochem. Photobiol. A* **364**, 433–442 (2018)
61. L. Liu, Controllable ZnO nanorod arrays@carbon fibers composites: towards advanced CO<sub>2</sub> photocatalytic reduction catalysts. *Ceram. Int.* **42**(10), 12516–12520 (2016)
62. I. Ahmad, The excellent photocatalytic performances of silver doped ZnO nanoparticles for hydrogen evolution. *SN Appl. Sci.* **1**, 327 (2019)
63. K.G. Kanade, Self-assembled aligned Cu doped ZnO nanoparticles for photocatalytic hydrogen production under visible light irradiation. *Mater. Chem. Phys.* **102**(1), 98–104 (2007)
64. I. Ahmad, Auto-combustion synthesis and photocatalytic hydrogen evolution activity of Al and Ni co-doped ZnO nanoparticles. *J. Ovonic Res.* **15**(1), 1–13 (2019)

**Publisher's Note** Springer Nature remains neutral with regard to jurisdictional claims in published maps and institutional affiliations.